Filatov, M. A.; Karuthedath, S.; Polestshuk, P. M.; Callaghan, S.; Flanagan, K. J.; Telitchko, M.; Wiesner, T.; Laquai, F.; Senge, M. O. (2018):
Control of triplet state generation in heavy atom-free BODIPY–anthracene dyads by media polarity and structural factors.
Physical Chemistry Chemical Physics 20, 8016–8031. doi: 10.1039/C7CP08472B

Control of triplet state generation in heavy atom-free BODIPY-anthracene dyads by media polarity and structural factors

Mikhail A. Filatov,[a*,Δ] Safakath Karuthedath,[b] Pavel M. Polestshuk,[c] Susan Callaghan,[a] Keith J. Flanagan,[a] Maxime Telitchko,[a] Thomas Wiesner,[a] Frédéric Laquai[b] and Mathias O. Senge[a*]

Abstract

A family of heavy atom-free BODIPY-anthracene dyads (BADs) exhibiting triplet excited state formation from charge-transfer states is reported. Four types of BODIPY scaffolds, different in the alkyl substitution pattern, and four anthracene derivatives have been used to access BADs. The fluorescence and intersystem crossing (ISC) in these dyads depend on donor-acceptor couplings and can be accurately controlled by the substitution or media polarity. Under conditions that do not allow charge transfer (CT), the dyads exhibit fluorescence with high quantum yields. Formation of charge-transfer states triggers ISC and the formation of long-lived triplet excited states in the dyads. The excited state properties were studied by steady-state techniques and ultrafast pump-probe spectroscopy to determine the parameters of the observed processes. Structural information for various BADs was derived from single crystal X-ray structure determinations alongside DFT molecular geometry optimization, revealing the effects of mutual orientation of subunits on the photophysical properties. TD-DFT calculations showed that alkyl substituents on the BODIPY destabilize local excited states (LE) and CT states in the dyads, thus controlling the charge transfer between the subunits. The effect of the dyad structure on the ISC efficiency was considered at CASSCF(4/4) level of theory and a correlation between mutual orientation of the subunits and the energy gap between singlet and triplet CT states was found.

Introduction

Boron dipyrromethene (BODIPY) dyes[1] represent one of the most actively studied classes of organic chromophores today. Ease of synthesis and derivatization, alongside tunability of their photophysical properties, make them attractive as materials for various uses. Most of these applications utilize the strong fluorescence of the BODIPY, e.g., for labeling of biomolecules,[2] as fluorescent switches,[3] chemosensors,[4] and laser dyes.[5] Currently, attention focusses on the generation of triplet excited states in BODIPYs due to emerging applications in photodynamic therapy (PDT),[6] photocatalysis,[7] and triplet-triplet annihilation photon up-conversion.[8]

A general approach towards BODIPY triplet sensitizers, which involves introduction of heavy atoms (typically halogen atoms or transition metals) into the molecule, that promotes spin-orbit coupling and thus enhances intersystem crossing, was discussed in a recent review.[9] Among the methods to facilitate triplet state formation in heavy atom-free chromophores using a spin converter,[10] exciton coupling,[11] doubly-substituted excited states[12] and twist-induced[13] ISC were studied in detail. However, the insufficient versatility of such methods is still a major limitation in the design of new generation triplet sensitizers.

Triplet state generation via photo-induced electron transfer (PeT) is a relatively well-known phenomenon which, however, has not been employed for the development of practical triplet sensitizers until very recently. PeT leads to the formation of charge-transfer states (CT) consisting of the donor radical-cation and the acceptor radical-anion which recombine to the ground state *via* different pathways. As has been noted in numerous works, CT state recombination may result in the formation of a local triplet excited state of either donor or acceptor, which further decays to the ground state either *via* phosphorescence or non-radiative decay process.[14] For instance, the generation of triplet excited states in heavy-atom–free donor−acceptor perylene bisimides dimers[15] and dyads[16] has been the subject of rigorous investigations by Wasielewski and co-workers. In these systems the triplet excited states were found to be generated *via* radical pair intersystem crossing (RP-ISC) or spin-orbit charge-transfer (SOCT-ISC) mechanisms from the CT state.

It could be expected, that, if the yield of the triplet excited states formed from a CT state is reasonably high and the resulting triplets possess long lifetimes, these systems can be applied as practical triplet sensitizers. Recently, we reported for the first time efficient triplet state generation in heavy atom-free BODIPY-anthracene dyads (BADs), mediated by PeT. BODIPY triplet states in these dyads are formed in high yields (up to 80%) and are rather long-lived (>40 μs). Moreover, water-soluble BAD derivatives were found to generate triplet states in biological media, resulting in singlet oxygen formation and causing strong cytotoxic effects under light irradiation.[17] Ease of synthesis and derivatization makes BADs promising for a wide range of applications. Subsequently, Zhao *et al.* reported that BADs can be employed as sensitizers for triplet−triplet annihilation up-conversion, providing high efficiency of the process.[18]

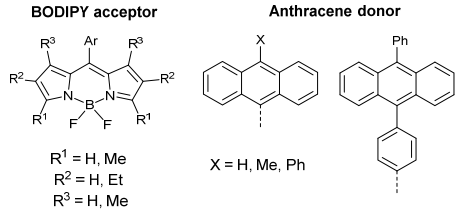

Figure 1. General structure of BODIPY-anthracene dyads studied in this work.

The key advantage of PeT-mediated triplet sensitization is the possibility of controlling the ratio between ISC efficiency and fluorescence emission of the dye. It is well-known that due to its high dipole moment the energy of CT states strongly depends on the polarity of the media. In non-polar solvents the CT energy level is usually significantly higher than the first excited state of the dyad, resulting in very low PeT efficiency and strong fluorescence. Conversely, in solvents possessing sufficient polarity, the CT state energy is reduced, making PeT and triplet state generation feasible. Moreover, PeT in donor-acceptor dyads can

[a] School of Chemistry, SFI Tetrapyrrole Laboratory, Trinity Biomedical Sciences Institute, 152-160 Pearse Street, Trinity College Dublin, The University of Dublin, Dublin 2, Ireland
[b] King Abdullah University of Science and Technology (KAUST), KAUST Solar Center (KSC), Physical Sciences and Engineering Division (PSE), Material Science and Engineering Program (MSE), Thuwal 23955-6900, Kingdom of Saudi Arabia
[c] Department of Chemistry, M.V. Lomonosov Moscow State University, Leninskie Gory, 1/3 Moscow 119991, Russia
* Corresponding authors. E-mail: mikhail.filatov@dit.ie; sengem@tcd.ie
Δ New address: School of Chemical and Pharmaceutical Science, Dublin Institute of Technology, Kevin Street, Dublin 8, Ireland

be switched on-off in response to complexation with metal ions, changes in pH, hydrogen bonding and other stimuli,[19] providing a tool to control intersystem crossing.

Although many BODIPY compounds were shown to exhibit PeT when combined with appropriate electron donors or acceptors,[20] observations of efficient formation of long-lived triplet states in such systems are scarce. Among those are BODIPYs with appended transition metal complexes,[21] dyads containing fullerene,[22] quinone[23] or methylpyridinium[24] as electron acceptors and BODIPY dimers.[25] For instance, recently reported BODIPY dyads bearing an extended acridinium cation as an electron donor showed triplet excited state yield of up to 15%.[26] It is still unclear which factors govern ISC efficiency in CT states. To further advance applications of heavy atom-free PeT sensitizers, insight to their photophysical characteristics and guidelines for the design of new material systems are required. With this in mind, we investigated the relationship between molecular structure, the efficiency of triplet state generation, and $^1O_2$ formation in a family of BADs (Fig. 1), varying in substitution patterns, molecular geometries and electronic coupling between the donor and acceptor subunits.

In this study, we particularly focused on unveiling the excited-state properties of the dyads, specifically PeT and triplet state generation. For this purpose, we studied the BADs using steady-state and ultrafast transient absorption spectroscopy. Secondly, we investigated singlet oxygen generation facilitated by the dyads in polar and non-polar solvents. Structural information for various dyads was obtained by single-crystal X-ray crystallography and molecular geometry optimization. Our major finding is that both, the solvent polarity and the substitution pattern of the BODIPY subunit can control triplet state generation in BADs. We found that dyads containing alkyl substituents on the BODIPY subunit are capable of triplet state formation, however, only in polar solvents. On the other hand, unsubstituted dyads were found to undergo PeT, generate triplet states, and produce $^1O_2$ both, in polar and non-polar media. To rationalize the observed properties we employed quantum-mechanical calculations, which identify the pathways of triplet state generation from CT states in the different types of dyads. This allowed us to elucidate the role of local excited states and CT state energies, and the role of mutual electron donor to electron acceptor orientations in the ISC process.

Results and Discussion

Design of the dyads

To systematically investigate the PeT and triplet state generation processes in BADs, we synthesized various dyads in which the highest occupied molecular orbital energy levels of the subunits are tuned systematically over a wide range. A previous report suggested that energies of the frontier orbitals in the BODIPY chromophore can be tuned by the introduction of alkyl groups.[27]

According to our calculations, the energies of the BODIPY HOMO orbitals increase gradually when going from unsubstituted BODIPY to hexaalkyl-substituted ones, while the HOMO-LUMO gap in this series is steadily decreasing (Fig. 2). The overall change in HOMO energies is rather considerable, suggesting that in the dyad molecules such changes induced by alkyl groups must have a strong effect on the electron transfer process. The effect of the alkyl substituents on the electronic structure depends solely on the position and number of the substituents and is almost unaffected by the nature of the substituent (e.g., methyl or ethyl groups). On the other hand, a variation of the anthracene substitution pattern was found to induce only slight changes in MO energies. Based on the match between HOMO energy levels of the subunits it could be expected that electron transfer occurs in the corresponding dyads.

Steady-state absorption and emission properties of the dyads

The absorption and fluorescence emission parameters of BADs in a range of solvents are given in Table 1. For all compounds the absorption spectra show transitions associated with the two subunits, indicating weak coupling of the chromophores in the ground state (Fig. 3a). Upon changing the solvent polarity, the shape and maxima of the absorption bands undergo little change.

In contrast, the emission of BADs is significantly affected by the solvent polarity. The spectrum of the representative dyad **10** (Fig. 3a) in non-polar hexane (ε_r = 1.9) shows a fluorescence emission centered at 512 nm and is characterized by a Stokes shift of 7 nm, 6.5 ns lifetime, and a very high emission quantum yield (0.91). In line with previous reports,[1b]Error! Bookmark not defined.[b] this emission can be attributed to a transition from the BODIPY singlet excited state (S^{BDP}) to the ground state of the molecule, or "local emission" (from LE) of the BODIPY chromophore. In polar ethanol (ε_r = 24.3), a new broad and structureless band appears at 620 nm, accompanied by a remarkable drop in emission intensity and quantum yield to 0.005 (Fig. 3a). The relative intensity of this band with respect to the LE band becomes more pronounced in highly polar DMF (ε_r = 38.3), accompanied by a further drop of the emission quantum yield to 0.003 (Fig. 3b). At the same time, its maximum is shifted further to the red by 20 nm, indicating that the energy of the corresponding excited state strongly depends on the solvent polarity. Quenching of the emission in polar media is usually observed upon formation of exciplexes and twisted intramolecular charge-transfer states.[28] Red-shifted broad emission bands reported for various donor-acceptor systems were attributed to CT states transition into the ground state of the dyad.[29] Such emission is commonly very weak, consistent with the low quantum yields observed for **10** in polar solvents. Thus, the emission observed for **10** in polar solvents can be interpreted as a mixture of fluorescence from the LE and CT state, which is formed due to intramolecular electron transfer from the anthracene to the BODIPY subunit.

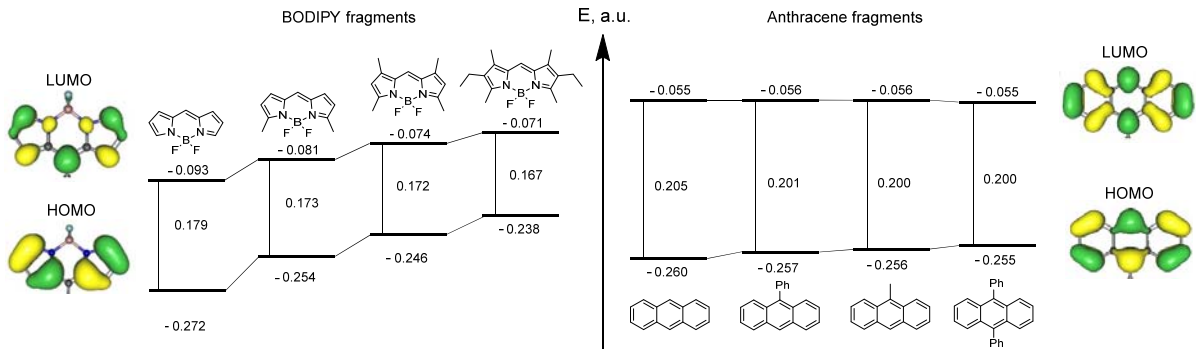

Figure 2. Molecular frontier orbital energies (values in atomic units) corresponding to HOMO and LUMO of the BODIPY and anthracene subunits in BADs.[30]

Table 1. Steady-state spectroscopic data for BADs in various solvents.

Compound (BAD)	Solvent[a]	λ_{abs} [b] (nm)	λ_{em} [b,c] (nm)	Φ_{em} [d,e]	Compound (BAD)	Solvent	λ_{abs} (nm)	λ_{em} (nm)	Φ_{em}
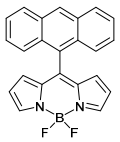 1	DMF	506	524, 738	<0.001	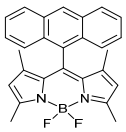 9	DMF	505	518, 615	0.011
	DCM	506	520, 706	0.002		DCM	506	517	0.072
	CH_3CN	502	519, 741	<0.001		CH_3CN	502	512, 621	0.006
	EtOH	503	520, 716	<0.001		EtOH	505	513	0.038
	toluene	508	525, 628	0.008		toluene	508	521	0.92
	hexane	505	521	0.135		hexane	504	515	0.99
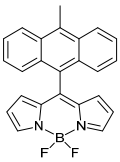 2	DMF	506	528	0.002	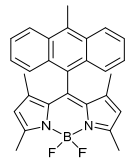 10	DMF	506	519, 612	0.003
	DCM	506	530	0.005		DCM	506	519, 643	0.011
	CH_3CN	502	528	0.001		CH_3CN	503	518, 654	0.002
	EtOH	503	528	0.002		EtOH	504	516, 627	0.005
	toluene	508	533	0.007		toluene	509	517	0.95
	hexane	504	566	0.041		hexane	505	512	0.91
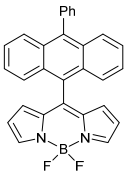 3	DMF	506	526, 716	0.001	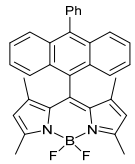 11	DMF	507	515, 621	0.01
	DCM	506	526, 727	0.002		DCM	507	515, 602	0.024
	CH_3CN	502	524, 702	0.001		CH_3CN	503	508,631	0.007
	EtOH	504	522, 716	0.002		EtOH	504	512, 606	0.02
	toluene	509	529, 636	0.007		toluene	509	519	0.79
	hexane	509	564	<0.001		hexane	505	514	0.90
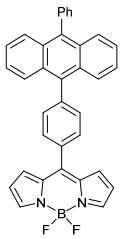 4	DMF	502	520	0.002	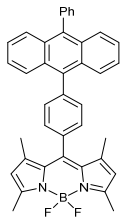 12	DMF	500	510	0.13
	DCM	502	518	0.002		DCM	502	512	0.57
	CH_3CN	498	516	0.001		CH_3CN	499	508	0.11
	EtOH	500	516	0.003		EtOH	500	510	0.37
	toluene	505	524	0.036		toluene	504	515	0.65
	hexane	501	517	0.014		hexane	502	511	0.70
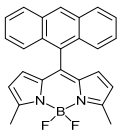 5	DMF	517	531, 671	0.003	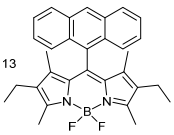 13	DMF	530	541	0.705
	DCM	518	528, 637	0.009		DCM	531	543	0.799
	CH_3CN	514	524, 678	0.002		CH_3CN	527	537	0.579
	EtOH	515	524, 634	0.005		EtOH	528	539	0.778
	toluene	519	530	0.29		toluene	533	544	0.806
	hexane	515	524	0.95		hexane	530	539	0.871
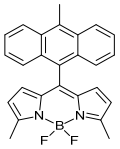 6	DMF	517	536, 716	<0.001	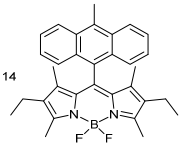 14	DMF	530	540	0.111
	DCM	517	536, 663	0.002		DCM	531	543	0.667
	CH_3CN	514	535, 724	<0.001		CH_3CN	527	538	0.054
	EtOH	515	533, 670	0.001		EtOH	528	538	0.314
	toluene	519	534	0.052		toluene	532	544	0.863
	hexane	515	525	0.37		hexane	529	540	0.883
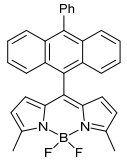 7	DMF	517	533, 676	0.004	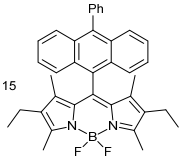 15	DMF	530	539	0.648
	DCM	518	533, 651	0.007		DCM	532	543	0.833
	CH_3CN	514	536, 715	0.004		CH_3CN	528	536	0.422
	EtOH	516	528, 652	0.006		EtOH	529	538	0.804
	toluene	519	532	0.141		toluene	534	544	0.858
	hexane	516	527	0.773		hexane	531	539	0.903
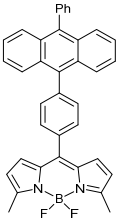 8	DMF	512	529	0.002	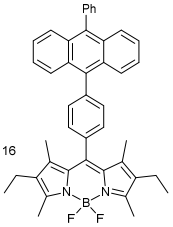 16	DMF	526	537	0.232
	DCM	513	526	0.027		DCM	527	540	0.744
	CH_3CN	508	523	0.002		CH_3CN	523	534	0.696
	EtOH	511	526	0.037		EtOH	525	537	0.841
	toluene	516	532	0.259		toluene	529	539	0.781
	hexane	512	526	0.204		hexane	526	536	0.756

[a] DMF – *N*,*N*-dimethylformamide, DCM – dichloromethane. [b] Absorption maxima corresponding to BODIPY chromophore are given. [c] The fluorescence was excited at the vibrational shoulder of the BODIPY absorption. Excitation wavelengths: 470 nm for dyads **1**-**4** and **9**-**12**, 480 nm for dyads **5**-**8**, 490 nm for dyads **13**-**16**. Emission spectra upon excitation in the region of anthracene absorption are given in Table S1 (SI). [d] The fluorescence quantum yields were measured using fluorescein disodium salt as a standard (Φ_{em} = 0.95 in 0.1 M NaOH).[31] [e] Represents integral emission coming from LE and CT excited states.

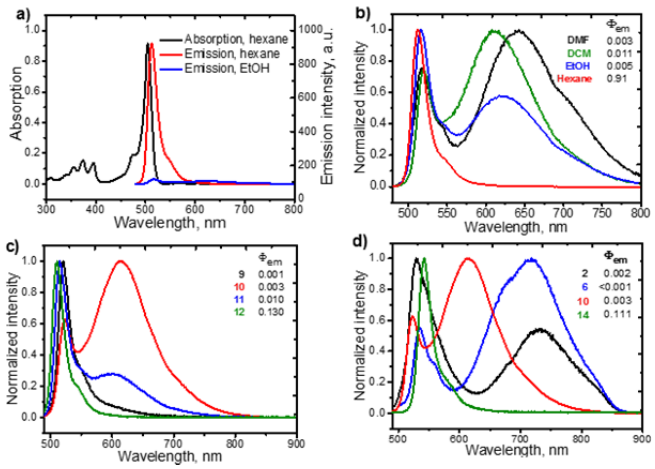

Figure 3. a) Absorption and emission spectra of **10** in hexane and EtOH. b) Normalized emission spectra of **10** in a range of solvents. c) Normalized emission spectra of dyads **9**, **10**, **11** and **12** in DMF. The emission was excited at 470 nm for all dyads. d) Normalized emission spectra of dyads **2** (λ_{exc} = 470 nm), **6** (λ_{exc} = 480 nm), **10** (λ_{exc} = 470 nm) and **14** (λ_{exc} = 490 nm) in DMF.

Changing the substitution pattern in the BODIPY or anthracene subunits has a strong effect on the spectroscopic properties of the dyads. Figure 3c shows the emission spectra of dyads **9**-**12**, possessing the same tetramethyl-substituted BODIPY scaffold, but four different anthracene moieties, in polar DMF. Dyads **9** and **11**, based on anthracene and 9-phenylanthracene, respectively, follow the characteristics observed for **10** and show a mixture of LE and CT emission. Integral emission quantum yields were found to be 0.011 and 0.01 for **9** and **11**, respectively, indicating very efficient PeT in these dyads. In contrast, in non-polar hexane these molecules exhibit very strong fluorescence from LE states with quantum yields of up to 0.99 (Table 1).

Dyad **12**, in which the anthracene moiety is not directly linked to the BODIPY, but separated *via* a phenylene bridge, exhibited different characteristics. In DMF, CT emission is not observed in the spectrum (Fig. 3c). However, the observed LE emission is substantially weaker (Φ_{em} = 0.13), than in non-polar hexane (Φ_{em} = 0.7). Likewise, the excited state lifetime in DMF is shorter (0.51 ns) than in hexane (8.2 ns). This indicates, that, although PeT takes place in dyad **12**, it is less efficient compared to the dyads with directly linked subunits. The rate of PeT is known to depend on the separation of the donor and acceptor subunits;[32] introduction of the phenylene spacer in **12** is likely to slow down the process.

The effect of the alkyl substitution pattern in the BODIPY on the emission properties is illustrated in Fig. 3d. Dyads **2**, **6**, **10** and **14** are composed of the same anthracenyl subunit (9-methylanthracene) and BODIPYs with different numbers (0 to 6) of alkyl-substituents, affecting the HOMO energy levels as illustrated in Figure 3. Dyads **2** and **6** show pronounced CT emission, substantially red-shifted compared to **10**, with maxima at 732 and 718 nm, respectively. Such a strong spectral shift may indicate enhanced electronic communication between the subunits, e.g., due to twisting.

On the other hand, the spectrum of **14** shows only LE emission indicating reduced PeT efficiency. The emission quantum yield of **14** in DMF and hexane was found to be 0.11 and 0.883, respectively. Thus, although PeT in **14** takes place, it is less efficient compared to the other dyads and strong LE emission from the BODIPY is dominating the spectrum. This situation is similar to the case of dyad **12**.

These observations indicate that the PeT efficiency can vary to a large extent in the dyads and depends on the electronic coupling between the subunits. To elucidate the structure-properties relationship, transient absorption spectroscopy measurements were performed (*vide infra*).

Singlet oxygen sensitization by BADs

Trapping of the photosensitized $^1O_2$ with 1,3-diphenylisobenzofuran was applied to measure Φ_Δ values in polar (ethanol) and non-polar solvents (hexane). As we previously described,[17Error! Bookmark not defined.] in certain cases the DPBF oxidation method overestimates the $^1O_2$ quantum yields of BADs, e.g., if chlorinated hydrocarbons are used as solvents. For instance, irradiation of oxygen-free solutions of BADs in dichloromethane results in a decrease of DPBF absorption. No reaction of DPBF with excited states of the dyads takes place under these conditions, as the absorption of BADs remains the same during the course of light irradiation. This result can be explained by photolysis of DPBF exposed to light in halogen-containing solvents in the absence of singlet oxygen, as described previously.[33] Due to this complication, quantum yields of singlet oxygen production in these solvents detected by DPBF can be significantly overestimated.

Table 2. Quantum yields of singlet oxygen photosensitization by BADs in ethanol and hexane.[a]

Compound	EtOH	Hexane
1	0.11	0.39
2	0.05	0.38
3	0.12	0.43
4	0.01	0.01
5	0.47	0.07
6	0.38	0.17
7	0.46	0.18
8	0.01	0.01
9	0.53	0.01
10	0.67	0.04
11	0.59	0.04
12	0.01	0.01
13	0.11	0.02
14	0.32	0.03
15	0.15	0.03
16	0.01	0.01

[a] Quantum yields were measured using DPBF as a $^1O_2$ trap and Rose Bengal as a reference photosensitizer (0.86 in ethanol).[34]

In contrast, when ethanol or hexane was employed as solvent no such effect was observed. The absorption of DPBF showed no changes upon irradiation of oxygen-free solutions under the same conditions (concentration, light intensity, degassing procedure). Alternatively, the addition of singlet oxygen quenchers (NaN_3 or amines) to the solutions terminated DPBF oxidation, confirming selective reaction of the trap with $^1O_2$ under these conditions.

As shown in Table 2, Φ_Δ values of BADs largely vary depending on the solvent and subunits structure. The highest values (up to 0.67) were observed for dyads **9**-**11**, based on tetramethyl-substituted BODIPY scaffolds, when ethanol was used as a solvent. This correlates with the photophysical data for these compounds given in Table 1, i.e. low emission quantum yields in polar solvents due to efficient PeT. Alternatively, in hexane these dyads showed low Φ_Δ values and, at the same time, high quantum yields of the fluorescence (>0.9), indicating low ISC values. In line with this, dyads **13**-**15** exhibited strong fluorescence in polar solvents and showed decreased Φ_Δ values.

Series **5**-**7**, based on the same 3,5-dimethyl-substituted BODIPY scaffold but with different anthracene units, showed slightly lower Φ_Δ values in ethanol (0.38-0.47), while a substantial increase of $^1O_2$ sensitization ability was observed in hexane.

Dyads **1**-**3**, lacking alkyl groups in the BODIPY showed the lowest values of Φ_Δ in ethanol (0.05-0.12) and, surprisingly high values in hexane (up to 0.43). Separation of the BODIPY and anthracene subunits *via* a phenylene spacer in dyads **4**, **8**, **12** and **16**, results in a drop of Φ_Δ to negligible values (0.01) in both solvents.

Femto- and nanosecond pump-probe transient absorption spectroscopy of BADs

To unravel the photophysical processes and charge transfer dynamics, two representative series of BADs were studied: 1) dyads **2**, **6**, **10,** and **14**, which contain the same anthracene subunit (9-methylanthracene), but with different BODIPY subunit alkyl substitution pattern (0, 2, 4 and 6 alkyl substituents) and 2) dyads **9**, **10**, **11,** and **12**, which are based on the same tetramethyl-substituted BODIPY, but carry different anthracene subunits. The dyads were excited at 355 nm, which selectively excites and populates the singlet state of the anthracene subunit. Based on a photophysical model established in our previous study,[17Error! Bookmark not defined.] we expected to observe a series of sequential processes reflected by equations (1)-(4).

$$Excitation\ at\ 355\ nm$$
$$S_0(Ant) + h\vartheta \rightarrow S_1(Ant^*) \quad \text{(Eq. 1)}$$
$$Energy\ transfer$$
$$S_1(Ant^*) \rightarrow S_1(BDP^*) \quad \text{(Eq. 2)}$$
$$Electron\ transfer$$
$$S_1(BDP^*) \rightarrow CT(BDP^- + Ant^+) \quad \text{(Eq. 3)}$$
$$CT\ \ recombination$$
$$CT(BDP^- + Ant^+) \rightarrow T_1(BDP^*) \quad \text{(Eq. 4a)}$$
$$CT\ recombination$$
$$CT(BDP^- + Ant^+) \rightarrow T_1(Ant^*) \quad \text{(Eq. 4b)}$$

Following excitation at 355 nm, singlet excited states of anthracene (S^{Ant}) undergo energy transfer (EnT) to BODIPY. EnT is followed by photo-induced electron transfer (PeT), generating charge-transfer states, equivalent to radical ion-pairs composed of anthracene radical-cations (Ant•+) and BODIPY radical-anions (BDP•−). The CT states then can undergo recombination to populate triplet excited states of either anthracene (T^{Ant}) or BODIPY (T^{BDP}).

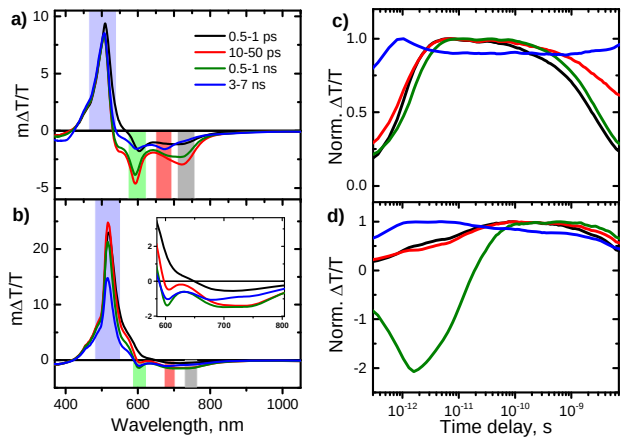

Figure 4. Picosecond-nanosecond transient absorption spectra of **10** measured in nitrogen at room temperature in DMF (a) and toluene (b) upon excitation at 355 nm with 100 fs pulses at various delay times as shown in the legend. Panels (c) and (d) show kinetics of selected spectral regions, as indicated by the vertical color bars in panel (a) and (b), respectively. The inset in panel (b) represents a zoomed-in region of the PA of **10** in toluene.

Figure 4 shows room temperature picosecond-nanosecond transient absorption spectra (a-b) and the corresponding kinetics (c-d) of **10** in DMF and toluene, respectively. Figure 4a represents the spectral response of **10** at different delay times varying from 300 fs to 7 ns. Anthracene singlet states were formed immediately after the excitation, and the associated decay of the 400 nm band and the concomitant rise of the photo bleach (PB) band of BODIPY at 510 nm indicates efficient EnT from anthracene to BODIPY.[Error! Bookmark not defined.] This ultrafast energy transfer from the anthracene to the BODIPY subunit yielded a singlet excited state of the BODIPY. The population of BODIPY singlet states, following excitation of the anthracene at 355 nm and successive EnT, was confirmed by steady-state fluorescence experiments, which showed fluorescence mainly from the BODIPY. For UV-Vis, steady-state emission and excitation spectra, we refer to Table S1 in the supporting information (SI).

After the ultrafast EnT was concluded, photo-induced absorption bands centered at 590 nm and 725 nm, belonging to BODIPY radical-anion and anthracene radical cation,[35] respectively were observed. These charge bands rose until ~50 ps and thereafter decayed with a half-life time of 3 ns. At later times, approximately 1 ns, the emergence of a band centered at 680 nm was observed. This band was assigned to anthracene radical-cations in line with assignments of this band in earlier reports.[36] We note that its presence exceeded the time window of our experiment. The kinetics of the 590 nm, 680 nm, and 725 nm band (Figure 4c) were comparable, indicating that they were caused by the same process. The band of Ant•+ at 680 nm overlapped with the BDP•− band and became more pronounced and visible at longer delay times.[37] The photo-induced absorption in the 380-420 nm region increased after several ps (not shown), which we assign to an overlap of absorption bands of the anthracene radical-cation and anthracene triplet states as BDP•− and BDP^3, followed entirely different kinetics.[38] Figure S9 compares the TA spectra and kinetics measured in air and nitrogen atmosphere.

To better understand the generation and deactivation pathways, exponential fits to the rise of the PB at 510 nm and PA at 725 nm were used, yielding time constants of 0.30 ps and 0.83 ps for the EnT and PeT processes, respectively. These rate constants are in good agreement with previously reported values.[39] The 590 nm band showed a small blue shift and slower rise at 570 nm with an inverse rate constant of 1.94 ps due to the generation of long-lived BODIPY triplet states by charge recombination, as previously reported.[17,18Error! Bookmark not defined.,Error! Bookmark not defined.] Kinetic traces of all PB and PA bands are shown in Figure 4c.

We further examined the femtosecond TA spectra of **10** in toluene (Figure 4b, and d). The spectral evolution following laser excitation at 355 nm differed remarkably from that observed in DMF solution. The immediate formation of the PB band of BODIPY with a rise time of 0.29 ps indicated that EnT was still efficient in this system. The PA bands rose much slower (~800 ps) and decayed to the ground state with negligible CT and triplet state formation. Unlike DMF, toluene has lower polarity, and thus the generated singlet states decayed to the ground state without forming CT states. The poor PeT was accompanied by a high fluorescence yield of the dyad in toluene (Table 1). Moreover, no rise of the PB band was observed at longer delay times, but a constant decay to the ground state. A bi-exponential fit to the decay of the PB gave inverse rate constants of 23 ps and 6.3 ns, respectively. Time-resolved photoluminescence (TR-PL) experiments showed a

mono-exponential decay with an inverse rate constant of 5.6 ns, well in line with the PB decay within the experimental error, indicating that the singlet states decayed to the ground states via fluorescence (see S1 for TR-PL spectra and kinetics of **10**). Comparing the ratio of PA and PB bands of the two samples (in DMF and toluene) demonstrated a remarkably different yield of the photo-generated states. The ratio of the band at 725 nm and corresponding PB showed a 32% yield in DMF solution, compared to a yield of only 5.6% in toluene. The value of the band at 590 nm compared to the PB was 50% and 5.5%, respectively, for DMF and toluene solutions. These observations confirmed that CT state recombination, rather than ISC from S_1 states, was responsible for triplet state formation in **10**.

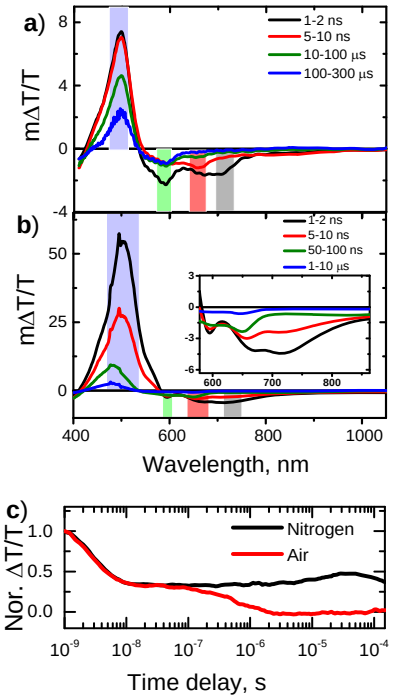

Figure 5. Nanosecond-microsecond transient absorption spectra of **10** in DMF (a) and in toluene (b). Different regions in the spectra are marked with vertical color bars. The inset of Figure 5b shows the zoomed-in region of the PA. Note that, clearly, before 10 μs, all excited states have decayed to the ground state. (c) Kinetics of the spectral region centered around 570 nm (green shaded in panel (a)) in nitrogen atmosphere (black) and in air-saturated conditions (red) of **10** in DMF, demonstrating triplet state quenching in the presence of oxygen.

To monitor the entire decay process of long-lived states, we performed TA experiments covering the nanosecond to microsecond time range. Figure 5 presents ns-μs TA spectra of **10** in DMF (a) and toluene (b), respectively, after laser excitation at 355 nm. As observed from the ps-ns spectra, the 590 nm band blue-shifted to 570 nm and showed a rise after 1 μs, indicating the generation of T^{BDP} as previously reported by us and others.[17,40] A mono-exponential fit to the rise of the triplet band yielded 13.2 μs. We confirmed the triplet generation by performing ns-μs TA in ambient air and observed substantial quenching of the 570 nm band (see Figure S9 for TA spectra). Figure 5c shows the decay dynamics of the 570 nm band in nitrogen and air-saturated conditions, as black and red lines, respectively. No rise in the decay dynamics was observed after 1 μs when measured in air-saturated conditions. Figure 5b presents the ns-μs TA spectra of **10** in toluene. The spectral dynamics followed the ps-ns TA spectra as described above. Although no noticeable rise due to the generation of triplets was observed, the TA in air-saturated solution showed quenching of the band around 570 nm (see Figure S9). The ratio of the PA at 590 nm to PB was determined to 15.5% and 0.8% for DMF and toluene solutions, respectively. This ratio was calculated by considering the maximum PA at 1 μs and the maximum PB at 1 ns. This indicates that triplet generation in toluene solution was strongly inhibited; in line with our photoluminescence studies (see Figure S1 for PL spectra and kinetics).

Figure 6 shows transient absorption spectra and kinetics of selected spectral regions for compound **6**. The spectral shape was identical to that of **10**, but the kinetics were largely different. In Figure 6a-c, no ultrafast generation of BODIPY singlets was observed due to a slower EnT with an inverse rate constant of 0.69 ps. The BDP•− band at 590 nm showed a rise until 3 ps, followed by a blue shift, and peaked at 570 nm as in the case of **10.** A mono-exponential fit to the rise of the band at 590 nm gave an inverse rate constant of 0.92 ps, indicating effective PeT in this system. Remarkably, the spectral bands started to decay rather quickly after ~50 ps with decay rates of 0.92 ns, 0.83 ns, and 0.79 ns for 515 nm, 590 nm, and 725 nm, respectively. As observed for **10**, the anthracene radical-cation at 680 nm became more evident at longer delay times and it decayed slower compared to the other bands.

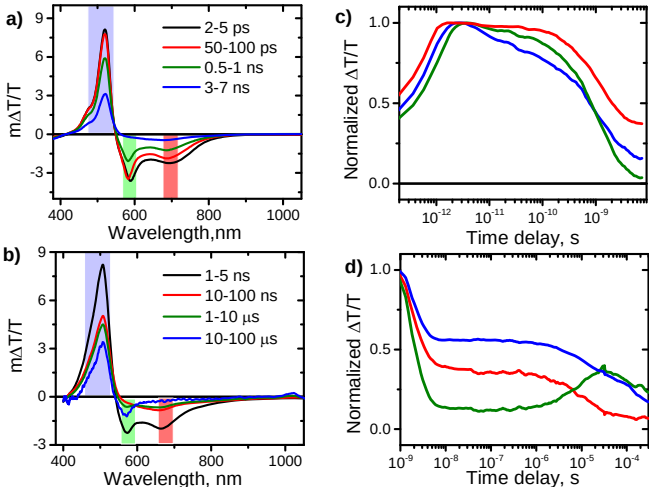

Figure 6. (a) Picosecond-nanosecond TA spectra of **6** in DMF measured under nitrogen atmosphere at room temperature upon excitation at 355 nm with 100 fs pulses at various delay times as indicated in the legend. (b) Nanosecond-microsecond transient absorption spectra of **6**. Panels (c) and (d) show kinetics of selected spectral regions, as indicated by vertical color bars in panels (a) and (b), respectively.

Table 3. Energy transfer rate, photoinduced electron transfer rate, and BDP triplet generation rate for BADs in DMF.

Compound	**EnT** rate	PeT rate	T^{BDP} rate
6	0.69±0.04 ps	0.92±0.02 ps	6.67±0.2 μs
9	1.06±0.15 ps	2.4±0.04 ps	6.23±0.1 μs
11	0.35±0.05 ps	0.85±0.05 ps	18.2±1μs
14	0.42±0.001ps	5.8±0.2 ps	16.7±2μs

Figure 6b shows ns-μs TA spectra of **6**. A fast decay followed by a rise of the 590 nm band (see the green vertical bar in panel (b)) with a rise time of 6.7 μs was assigned to triplet generation by charge recombination. The presence of triplets was confirmed by measuring TA in air-saturated solutions as in the case of **10**. For

the complete spectra and kinetics of **6**, we refer to S10. The ratio of the 590 nm band compared to the PB band was 14%, which was comparable to that of **10** (in DMF). Comparable spectral and kinetics features were observed for the other dyads, namely **9**, **11** and **14**. Table 3 shows the EnT, PeT and triplet generation rates for these dyads. They demonstrated spectrally similar responses upon exciting with a 355 nm laser pulse at room temperature. Among these four dyads, **11** showed fastest EnT and PeT. All relevant spectral and kinetic information for the samples listed in Table 3 can be found in the SI (figures S10-S14). For TR-PL spectra and kinetics, we refer to Figures S2-S5.

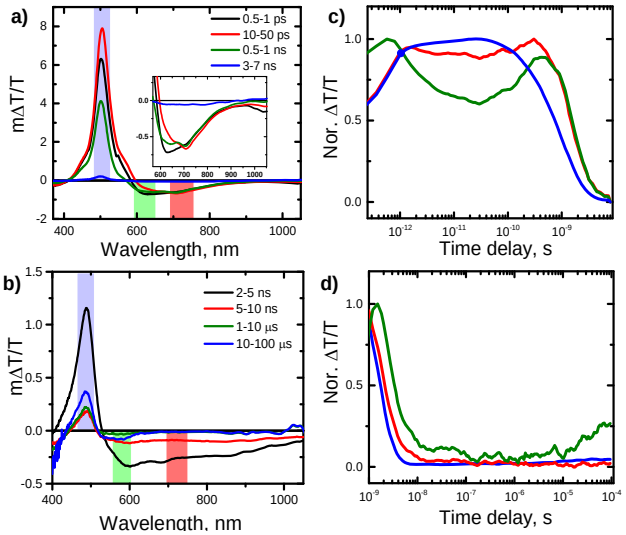

Figure 7. (a) Picosecond-nanosecond transient absorption spectra of **12** in DMF, measured under nitrogen atmosphere at room temperature following excitation at 355 nm with 100 fs pulses at various delay times as indicated in the legend. (b) Nanosecond-microsecond transient absorption spectra of **12** under the same condition as in panel (a). Panels (c) and (d) show kinetics of the corresponding selected bands, as indicated by vertical color bars in panels (a) and (b), respectively.

Figure 7 illustrates transient absorption spectra and kinetics of dyad **12**. As seen from Figure 7a and c, the PB band at 510 nm exhibited a fast rise followed by a slow growth, indicating efficient EnT, but poor PeT in this molecule. The spectral characteristics are reminiscent of **10** in toluene, where PeT was suppressed due to the low polarity of the solvent. Interestingly, both PA bands (590 nm and 725 nm) showed a small rise after 100 ps due to less efficient PeT. Almost 90% of the PB disappeared within a few nanoseconds, demonstrating only minor formation of long-lived charge-transfer states after photoexcitation. The inset of Figure 7a shows a zoomed-in image of the PA region, which exhibited a slow rise and subsequent fast decay to the ground state. Mono-exponential fits gave inverse rate constants of 0.60 ps and 0.59 ps for the PB and PA bands, respectively, indicating that the PA mostly originated from singlets generated via EnT. ns-μs Transient absorption spectroscopy results obtained on **12** are shown in Figure 7b and d. A monotonous decay of the PB was observed until 1 μs followed by a growth in line with the rise of the 590 nm band, caused by the formation of triplets. The ratio of the 590 nm band to the PB was 0.7%, far less than that of **10** in DMF, indicating very inefficient triplet generation. For the complete comparison of spectra and dynamics of **12** we refer to Figures S15 and 16 in the supporting information. S6 shows complete TR-PL spectra and kinetics of **12**.

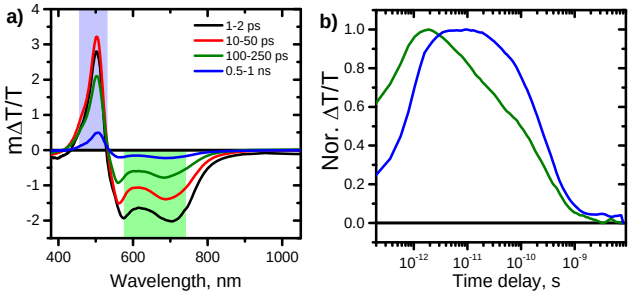

Figure 8. (a) Picosecond-nanosecond transient absorption spectra of **2** in DMF measured under nitrogen atmosphere at room temperature upon excitation at 355 nm with 100 fs pulses at various delay times as indicated in the legend and (b) kinetics of the corresponding bands, as indicated by vertical color bars.

In Figure 8, ps-ns TA spectra and corresponding kinetics of **2** (DMF) after 355 nm excitation are shown. Unlike the case of **10**, here PB and PA bands decayed to the ground state within few nanoseconds. Although the extracted rate of EnT (0.55 ps) indicated fast energy transfer, the steady-state emission spectra (see Table T1 in the SI) showed that upon excitation at 355 nm, the resulting emission originated mainly from the anthracene unit. Thus, it appears that unlike for the other dyads, upon 355 nm excitation of **2**, the population of BODIPY singlet excited states was very limited. However, it can be concluded that the CT state of **2** was short-lived compared to **10**, which in turn reduced the probability of generating triplet states. In **2,** 90% of the total excited state population decayed within 0.7 ns, whereas in **10**, more than 75 % were still present on this timescale. Hence, we excited **2** at 510 nm in the region of BODIPY absorption and compared the TA spectra of **2** in DMF and toluene.

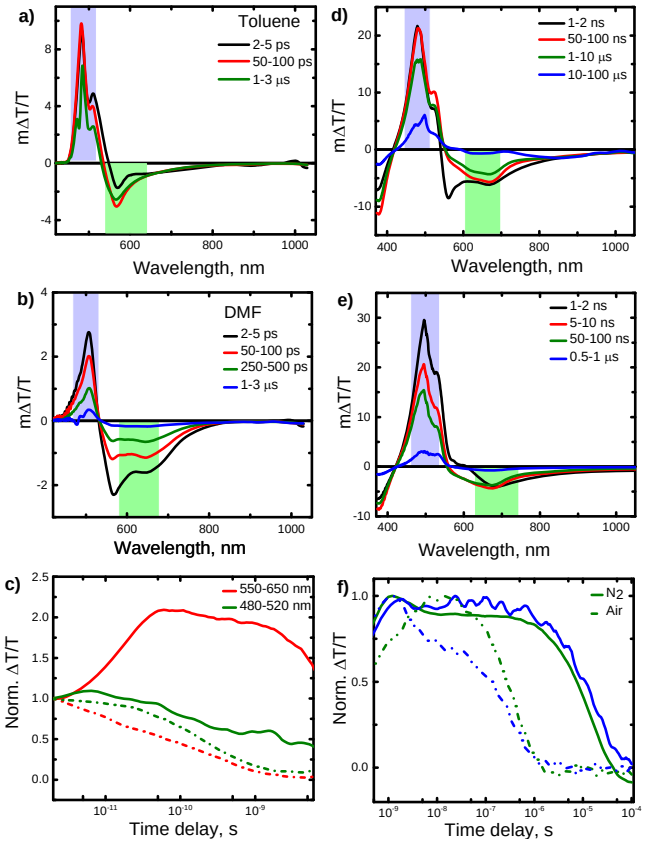

Figure 9. Picosecond-nanosecond TA spectra of **2** in (a) DMF, (b) toluene; kinetics of the bands indicated by vertical color bars are shown in panel (c) (dotted lines: DMF, solid lines: toluene). Panels (d) and (e) show nanosecond-microsecond TA spectra of **2** (toluene) measured under nitrogen atmosphere and in air-

saturated conditions, respectively. Panel (f) shows the nanosecond-microsecond kinetics of nitrogen (solid lines) and air-saturated (dotted lines) solutions of **2** for the vertical color bars indicated in panel (d) and (f).

Picosecond-nanosecond TA spectra of **2** in DMF and toluene after excitation at 510 nm are shown in Figure 9. The immediate difference was the presence of very long-lived states and the slow rise of the PA and PB bands of the sample measured in toluene. At 7 ns, (the longest delay we can achieve with our ps-ns TA setup), the 68% of the original PB band remained. In DMF, **2** did not generate a sufficient number of long-lived states. The PA band centered at 570 nm kept rising until 70 ps, followed by very slow decay. TA on air-saturated solutions showed no quenching of the long-lived states, indicating that no triplets were generated on this time scale (see Figure S17 for TA spectra in air). Surprisingly, we observed the efficient population of the T^{BDP} state in toluene. Figure 9c compares the kinetics of **2** in toluene (solid lines) and in DMF (dotted lines). In DMF, **2** showed a monotonous decay to the ground state without any signature of triplet formation, whereas in toluene, generation of long-lived BODIPY triplet species was clearly observed. Since the excited state population was very long-lived, we performed nanosecond-microsecond TA to monitor their decay dynamics. S7 shows TR-PL spectra and kinetics of **2**.

Panels (d) and (e) in Figure 9 show ns-µs TA spectra of **2** in toluene after excitation at 532 nm, measured under nitrogen atmosphere and in air, respectively. Three bands could be distinguished at early times from the ns-µs TA spectra, and were attributed to PB and triplet bands of BODIPY. Interestingly, even at 100 µs, a band around 820 nm existed, while other bands showed a monotonous decay. We note that the bands centered around 380-420 nm, 570-700 nm, and 780-820 nm showed similar decay dynamics and were substantially quenched upon air exposure (Figures 9d, e and f), confirming that all bands originate from BODIPY triplets. This implies, the excitation wavelength and solvents play a major role in the excited state dynamics of **2**. In fact, we assigned the 380-420 nm band to T^{Ant} in other dyads in DMF solution after selectively exciting the anthracene subunit. Here, we assumed that exciting anthracene would not lead to T^{BDP} and a feature at 380-420 nm, but instead would generate T^{Ant}, since the T^{BDP} at 570 nm shows different dynamics. However, Zhang *et al.* reported recently that the 380 nm band can be assigned to T^{BDP} created after excitation of anthracene,[41] which contradicts our results and those of others.[42] We note that the 380-420 nm band and its dynamics were quenched after 100 ns upon oxygen exposure, following anthracene excitation (at 370 nm). Additionally, we note that the triplet formation in toluene upon 532 nm excitation was faster than that in DMF solution (see S11).

Elucidation of the dyad solid state structures

Single crystals of the dyads suitable for X-ray crystallography were obtained by slow evaporation of BAD solutions in DCM, chloroform or toluene. For analysis, we investigated distortions of atoms from the least--squares--planes of the BODIPY and anthracene subunits (listed in Table 4), the carbon-carbon bond lengths of C8–C15 and the rotations around the C8–C15 bond designated as Ψ (Figure 10**)**.

Additionally, in the packing arrangement, we evaluated the packing type (head-to-head or head-to-tail), solvent effects, and the formation of any halogen short contacts between fluorine and hydrogen atoms (bond lengths given with respects to H···F distance and angles are quoted for C–H···F). The previously published structures of BADs **1** and **10** were included here for comparison. All structural features of interest are summarized in Table 4.

The BAD structures revealed a range of ψ rotations, as is illustrated in Figure 10. This suggests a relatively large degree of freedom of rotation is available around the C8–C15 bond. For directly-linked BODIPY-anthracene systems, the compounds studied here crystallized with an almost orthogonal (69-88°) orientation (Table 4). The introduction of additional alkyl substituents into the BODIPY core resulted in a decrease of the C8–C15 bond length: from 1.499(1) Å in alkyl-unsubstituted **2** to 1.481(1) Å for the hexaalkyl-substituted dyad **14**. Upon changing the substitution pattern of the anthracene subunit, only a small variation in the C8–C15 bond length was noted. In comparison, the structure of **1**, with unsubstituted BODIPY and anthracene moieties, exhibited the largest C8–C15 bond length (1.501 Å).[43]

Two major forms of crystal packing were found for the BAD systems. The first is the head-to-head arrangement, as for **2** (Figure S28). This is strongly favored due to the formation of a dimer *via* two C–H···F halogen bonds, C5_1–H5_1···F13 (2.181(1) Å and 145.0(1)°) and C5_2–H5_2···F14 (2.498(8) Å and 154.1(1)°). Dyads **7** (Figure S29) and **14** (Figure S30) feature a predominantly head-to-head overlapped structure, aided by short contacts between the fluorine atoms of the BODIPY and anthracene subunit. In **14**, a C–H···F short contact is seen between C26–H26···F14 (2.479(1) Å and 157.2(1)°). This is commonly referred to as the 2-position of the anthracene subunit and preserves the head-to-head structure in the crystal packing. Dyad **7** displays a similar packing to **14**; however, in this case, the short C–H···F contact is present between C17–H17···F13 (2.309(1) Å and 167.9(1)°), which is commonly referred to as the 1-position of the anthracene subunit.

The crystal structures **10** and **10-T** are isostructural, varying only by the inclusion of a toluene molecule that resulted in ~1 Å increase in the a-axis of the unit cell for **10-T**. The inclusion of toluene prevents formation of a head-to-head dimer, observed in the previously published structure of **10**, and favors a head-to-head overlap. This is aided by a short contact between the C24–H24···F14 (2.579(2) Å, 125.7(1)°) and C25–H25···F14 (2.639(1) Å, 122.5(1)°) for **10-T**. C25 is commonly referred to as the 4-position of the anthracene unit. Similarly, in compound **10**, the presence of a short contact between C26–H26···F14 (2.329(1) Å and 132.1(1)°), which is considered the 2-position of anthracene, is observed. Additionally, **10** shows a short contact between C31–H31C···F14 (2.517(1) Å and 121.1(1)°), which forms the head-to-head dimer. Due to the presence of toluene in **10-T**, this feature is removed as the major packing motif due to the toluene molecule occupying the space previously occupied by the anthracene subunit.

The second type of packing is a head-to-tail arrangement within the unit cell. This is the main feature observed for **5** (Fig. S32), **6** (Fig. S33) and **10** (Fig. S34-35). The packing of **5** displays a highly ordered fluorine···hydrogen short contact network within the packing of molecules in the unit cell. This results in two close contacts between C22_1–H22_1···F13_1 and its symmetry equivalent C22_1–H22_1···F13_1 (2.491(2) Å and 152.8(3)°), forming a bifurcated interaction between the BODIPY and the 10-position of the anthracene unit. This feature is singular to compounds **5** and **1**, due to the presence of methyl or phenyl moieties on the 10-position of the remaining anthracene units within this set. When compared to the published structure of **1**, we can see this type of H···F interaction is favored, provided the anthracene subunit is unhindered. Additionally, the presence of a close contact between C23_1–H23_1···F13_2 (2.418(2) Å and 172.9(1)°) facilitates a H···F close contact system between neighboring molecules related by an almost orthogonal rotation. Dyad **6** shows a packing independent of close contacts between

H···F, in which the BAD units are in a head-to-tail orientation. This is due to the presence of a methyl group which shields the fluorine atoms from forming close contacts with the methyl-substituted anthracene unit, as compared to the other BAD systems shown (Fig. S33).

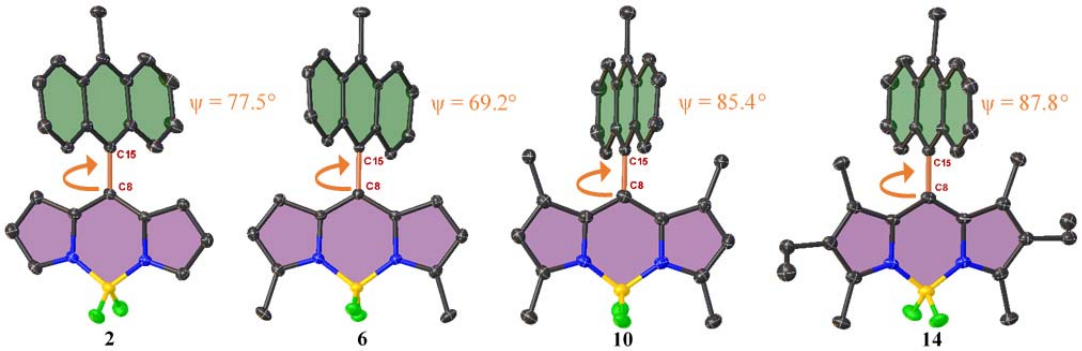

Figure 10. Structural features of the dyads under investigation. Orange denotes the bond used to C8–C15 bond length. ψ-angle rotations were determined by measuring the dihedral angle between the anthracene (green) and BODIPY (purple) least-squares-plane. Thermal ellipsoids displacement show 50 % probability, hydrogen atoms have been omitted for clarity.

Table 4. Selected structural details of twist angle, bond length and deviations from planarity in the dyads studied.

Compound	ψ (°)[a]	C8–C15 (Å)	ΔB (Å)[b]	ΔA/P (Å)[c]
1[d]	81.5(1)	1.501(2)	0.035	0.041
2[e]	77.5(1)	1.499(1)	0.036	0.016
	73.9(1)	1.499(1)	0.126	0.074
5[e]	75.3(4)	1.505(1)	0.020	0.025
	81.2(6)	1.493(1)	0.014	0.012
6	69.2(3)	1.494(1)	0.026	0.057
7	86.7(2)	1.496(1)	0.041	0.015
8[f]	42.0(1)	5.804(1)[f]	0.067	0.026
	53.0(1)	5.798(1)[f]	0.071	0.043
10	78.3(5)	1.492(1)	0.066	0.028
10-T[g]	85.4(6)	1.492(1)	0.070	0.011
14	87.8(3)	1.481(1)	0.015	0.030

[a] Dihedral angle between the mean planes of the BODIPY and 8-substituent (anthracene or phenylene). [b] Deviation of atoms from the mean plane of the BODIPY. [c] Deviation of atoms from the mean plane of the anthracene. [d] Described in reference **Error! Bookmark not defined.**. [e] Two independent molecules in the asymmetric unit and both structural factors are reported. [f] Separation between the anthracene and BODIPY moieties was measure by taking the distance between C8 and C21 due to the presence of a phenyl spacer unit. [g] Isostructural to **10**, however, includes toluene molecules of solvation.

The structure of dyad **8** (Fig. 11), in which a phenylene spacer is positioned between the BODIPY core and anthracene subunit, displays a significantly decreased ψ-angle of 42.0(1) and 53.0(1)° in comparison to the BAD systems outlined above. It features one of the shortest C8-C15 bond lengths with 1.484(2) and 1.486(2) Å for both independent molecules. However, it should be noted that due to the phenylene spacer, **8** displays the largest distance between the BODIPY core (C8) and the anthracene subunit (C21) of 5.798(1) and 5.804(1) Å. It features a predominantly head-to-head overlapping crystal structure (Fig. S31) aided by short contacts between the fluorine atoms of the BODIPY and anthracene or terminal phenyl subunit. The structure of **8** shows a similar head-to-head overlap as seen in **7** with C33_1–H33_1···F14_1 (2.602(3) Å and 142.5(1)°), with both compounds **7** and **8** interacting with the 1-position of the anthracene moiety. However, as two independent molecules are present in the asymmetric unit, a second C–H···F is present between the BODIPY and the terminal phenyl, C39_2–H39_2···F14_2 (2.405(4) Å and 167.4(2)°), Fig. S31.

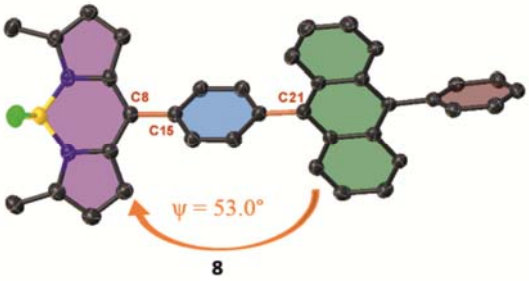

Figure 11. Structural features in the molecular structure of **8**. Separation between the anthracene and BODIPY moieties was measure by taking the distance between C8 and C21. ψ-angle refers to the dihedral angle between the anthracene (green) and BODIPY (purple) least squares plane. Thermal ellipsoids displacement show 50 % probability, hydrogen atoms have been omitted for clarity.

In conclusion, the ψ-angle in the solid state depends on the environment (i.e. the substitution pattern) around both the BODIPY and the 8 ('meso')-residue. The introduction of methyl groups at the anthracene 10-position facilitates head-to-head dimer formation, while the introduction of methyl groups at the C3 and C5 positions make this interaction less favorable. The inclusion of solvents, while not always having the largest effect on the overall packing (changing head-to-head to head-to-tail, or *vice-versa*) leads to inclusion of solvent molecules in pockets that would have been previously been occupied by the meso-substituent as in the case of **10** and **10-T**. Throughout these systems, compounds containing C3- and C5-substituents always presented H···F intramolecular contacts with the methyl substitutions and fluorine atoms.

Effect of alkyl substituents and solvent polarity on charge transfer

In order to understand the effect of alkyl substituents in controlling the properties of BODIPYs, a comparative computational study was performed.

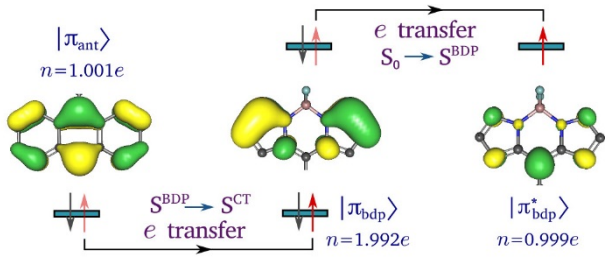

Figure 12. Scheme of electronic transitions corresponding to $S_0 \rightarrow S^{BDP}$ and $S^{BDP} \rightarrow S^{CT}$ interconversions. Surfaces correspond to CASSCF(4/4) natural orbitals involved in these processes with respective occupation numbers (*n*) are depicted.

The first excited state S^{BDP} in the studied molecules arises from local $\pi_{BDP} \rightarrow \pi^*_{BDP}$ excitation on the BODIPY fragment. This excitation was characterized by the TDDFT/M06-2X method to possess an oscillator strength of 0.5. In order for PeT processes from the anthracene (π_{Ant}) to the BODIPY (π_{BDP}) fragments to occur after $S_0 \rightarrow S^{BDP}$ excitation it is essential that the charge-transfer state S^{CT} is energetically close to S^{BDP}. These processes are illustrated in Fig. 12.

Two main factors govern the excitation energy of S^{CT}. First, the effect of alkyl substituents on E_{HOMO} and E_{LUMO} of both subunits and the CT state. The data shown in Fig. 2 demonstrate the destabilizing effect of alkyl substituents on the HOMO and LUMO energies of the subunits. In the S^{CT} state the BODIPY fragment accepts an electron to form the $BDP^{\bullet -}$ species and thus, the addition of electron donating alkyl groups inevitably increases the energy of the S^{CT} state. Consequently, this hinders the electron transfer from anthracene to the BODIPY subunit. The data in Table 5 include the energies of S^{CT} states for a series of substituted systems and fully confirm the conclusion given above.

Table 5. DFT-SCF computed excitation energies of the dyad's S^{CT} states and the energy gap between the S^{BDP} and S^{CT} states, $E[S^{CT}-S^{BDP}]$, in vacuum and ethanol. All data are given in eV.

Dyad	$E(S^{CT})$ Vacuum	$E(S^{CT})$ EtOH	$E(S^{CT})-E(S^{BDP})$ Vacuum	$E(S^{CT})-E(S^{BDP})$ EtOH
1	2.86	2.18	0.43	– 0.24
2	2.75	2.07	0.32	– 0.35
5	3.03	2.38	0.70	0.06
6	2.92	2.27	0.59	– 0.05
9	3.23	2.57	0.85	0.19
10	3.11	2.46	0.73	0.08
13	3.26	2.62	0.98	0.33
14	3.15	2.52	0.86	0.24

The second factor influencing the excitation energy of S^{CT} is the dielectric susceptibility of a medium or, in other words, the solvent polarity. In the CT state two separated electrons are located on the anthracene and BODIPY subunits, thus leading to a very large dipole moment that is computed to be μ = 17-19 D *in vacuo*, which is much larger than that for the valence S^{BDP} state (5 D). It is well known that in non-polar media CT cannot be stabilized *via* electrostatic interactions with solvent molecules, resulting in its energy being far above that of S_1^{BDP}. This makes PeT between the subunits inefficient and results in the dyad becoming a strong fluorophore. Interactions with polar solvent molecules strongly stabilize the CT state by about 0.7 eV (Table 5). Thus, the stabilized S^{CT} state is close in its energy to S^{BDP}, with an energy gap between the states of around 0.1-0.4 eV. In polar solvents the $S^{BDP} \rightarrow S^{CT}$ transition can be observed even for dyads with alkyl substituents, which destabilize the S^{CT} state. Note, that the probability of such a transition in polar solvents is subtly reduced for dyad **2** due to an increase in the separation energy gap (more than 0.3 eV, in reverse order) between the S^{BDP} and S^{CT} states (the latter is more significantly decreased in energy). Therefore, the $S^{BDP} \rightarrow S^{CT}$ transition for alkyl-substituted dyads can efficiently take place only in highly polar solvents, but in the case of alkyl-unsubstituted systems, the apolar environment allows such a process. This conclusion is fully supported by the energy separation gaps observed between these two states presented in Table 5. Thus, the probability of the $S^{BDP} \rightarrow S^{CT}$ transition reduces upon increasing the energy gap between LE and CT states ($E[S^{CT}] - E[S^{BDP}]$). The singlet oxygen quantum yields are in full agreement with these conclusions. The dependence of the measured Φ_Δ on the computed difference between S^{CT} and S^{BDP} states energies is given in Figure 13. Two branches are observed: one corresponding to $E[S^{CT}] > E[S^{BDP}]$ (right branch), while the other relates to the $E[S^{CT}] < E[S^{BDP}]$ situation (left branch). Clearly, increasing the $E[S^{CT}] / E[S^{BDP}]$ gap leads to a subtle decrease of Φ_Δ, indicating the reduced probability of the $S^{CT} \rightarrow T^{CT}$ ISC process.

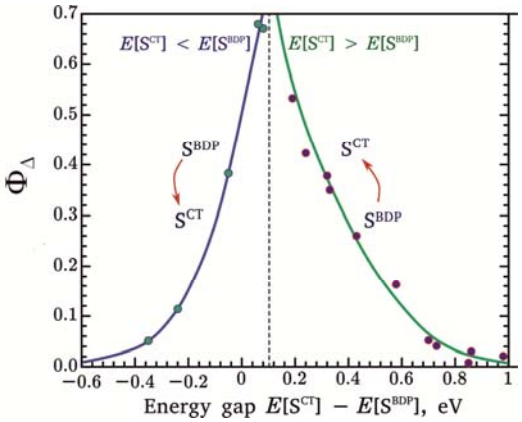

Figure 13. Dependence of Φ_Δ measured for BADs on the computed $E[S^{CT}] - E[S^{BDP}]$ values in EtOH.

Tentative intersystem crossing pathway in BADs

The calculations based on the M06-2X functional showed that the BODIPY and anthracene fragments are nearly orthogonal in all studied systems. According to the study of a potential energy surface along the dihedral angle between the fragments, at standard room temperature conditions can vary only in a limited range. For instance, in dyads **1-3**, based on unsubstituted BODIPY, the maximum achievable twist at room temperature is 60-65° (this corresponds to ~3-4 kcal/mol vibrational energy). Variable temperature ^{1}H NMR studies support that mutual rotation between the subunits is taking place in these dyads. A singlet at 6.38 ppm, corresponding to the pyrrolic protons in position 1 and 7 of the BODIPY core, was observed to split into a multiplet at lower temperatures (Fig. S38), while other pyrrolic protons are affected. In line with previous reports on BODIPY molecular rotors[44] such splitting is due to the restriction of rotation of anthracene rings. Additionally, substantially red-shifted CT emission of dyads lacking alkyl substituents in positions 1 and 7 of the BODIPY (Fig. 3d) evidences increased conjugation between the subunits which is achieved due to twisting.

The presence of alkyl substituents in the BODIPY restricts the maximal twisting angle to 80°. The geometries with lower angles possess substantially higher energies. Thus, it appears likely that the most favorable geometry of the dyads **9**-**11** and **13**-**15** (bearing alkyl substituents in positions 1 and 7) in solution is close to orthogonal, as was shown by XRD analysis (see above). For dyads **1**-**3** and **5**-**7** (no alkyl substituents in positions 1 and 7), with a

larger degree of rotational freedom along the C8-C15 bond, a range of conformations in solution can be expected. In the case of dyads **4**, **8**, **12** and **16**, containing phenylene bridges between the subunits, an almost free rotation with an angle of 55° corresponding to its lowest energy configuration can be expected.

It has been noted in a number of previous works that an orthogonal arrangement of the subunits in multichromophoric systems results in increased ISC. Particularly, orthogonal BODIPY dimers and trimers were reported by Akkaya *et al.* as efficient triplet sensitizers.[12a] However, the effect of orthogonal chromophore arrangement on ISC was attributed to a prevention of mixing of the π-systems of the two subunits, keeping HOMO and LUMO of the subunits essentially unperturbed. The present quantum chemical investigation, in conjunction with experimental photophysical data for BADs, shows that the orthogonal geometry is responsible for reducing the S-T energy gap in the CT state. Similar effects have recently been reported for donor-orthogonal-acceptor conjugated polymers[45] and OLED emitters exhibiting thermally-activated delayed fluorescence.[46]

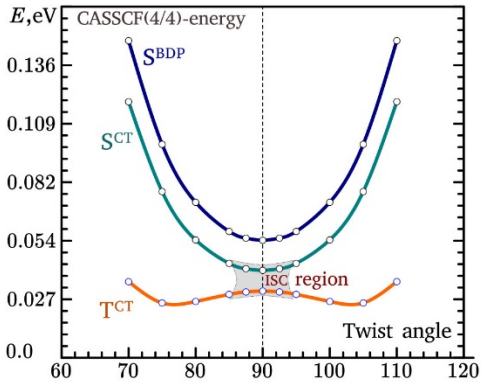

Figure 14. Frozen scan of PES for SBDP, SCT and TCT states along the twist angle.

The frozen scan for the simplest dyad **1** along the twist dihedral angle at CASSCF(4/4) level of theory is given in Fig. 14. Energies of singlet and triplet CT states strongly depend on the relative orientation of the donor and acceptor subunits, with the $\Delta E_{S\text{-}T}$ energy varying from 0.1 eV for a conformation with 80° twist between the subunits, to less than 0.01 eV for a dihedral angle larger than 80°. The near-orthogonality of the D–A units is thus key to achieving almost degenerate singlet and triplet levels. The closeness of S^{CT} and T^{CT} energies (they are almost degenerate) on the potential energy surface in the vicinity of orthogonal geometries (~70-100 cm^{-1}) opens the possibility for ISC to take place.

Two general mechanisms for ISC in the studied dyads can be considered: spin orbit coupling (SOC) and hyperfine coupling (HFC). However, if the dihedral angle between the subunits is close to 90°, SOC is not operative as the orbitals involved in both states are the same and thus the matrix element for the $S^{CT} \rightarrow T^{CT}$ transition approaches zero. Hence, no change in orbital angular momentum, as required for a spin flip, can occur.[47] However, the orthogonal geometry of the dyad subunits allows for efficient crossing between the S^{CT} state and an energetically close local triplet state – the T^{BDP} or T^{Ant} state in this case – *via* a spin orbit charge transfer ISC process, (SOCT), as this spin flip transition couples to a change in orbital angular momentum.[48] On the other hand, the process can take place due to the electronuclear hyperfine coupling in the two radical-ion fragments. Populated S^{CT} states may lead to ISC, thus producing the triplet T^{CT} electronic states, which then undergo spin-selective intersystem charge recombination to the S_0 ground state or pass through the triplet valence states T^{BDP} and T^{Ant}. Both HFC and SOCT have been proposed to be operative in donor-acceptor dyads.[49] However, this is still an open question and further investigations are needed to evaluate the role of HFC in BADs.

Thus, while the electronic coupling between the local singlet excited state of the BODIPY (S^{BDP}) and the charge-transfer singlet state (S^{CT}) are responsible for the efficiency of PeT, ISC in the BADs is controlled by the molecular geometry. In order to minimize the singlet–triplet energy gap the dyad's geometry has to be dynamically fluctuating about orthogonality. When the molecule is rigidly constrained in the orthogonal geometry (e.g., due to the presence of alkyl substituents on the BODIPY), the singlet–triplet gap in the CT state is minimized. In dyads **9**-**11**, efficient electron transfer provides high yields of CT, which, in conjunction with a near orthogonal geometry, results in efficient ISC and triplet state formation as evidenced by the TA studies and high Φ_Δ values. In contrast, while an orthogonal geometry is conserved for dyads **13**-**15**, the larger number of destabilizing alkyl groups lowers the efficiency of PeT and CT state yield resulting in a decrease of ISC and Φ_Δ values. In the absence of methyl substituents in positions 1 and 7 of the BODIPY, molecular vibrations allow a deviation from orthogonality for dyads **5**-**7**. Despite the high efficiency of PeT due to low $E(S^{CT})$-$E(S^{BDP})$ values, deviations from orthogonality lead to reduced triplet state yields in these dyads. A similar effect can be considered, if the subunits are separated by phenylene spacers, as in dyads **4**, **8**, **12** and **16**. Finally, for alkyl-unsubstituted dyads **1**-**4**, the geometry can relax towards non-orthogonality and as a result the singlet–triplet energy gap in CT state increases, preventing efficient ISC and the formation of local BODIPY triplet states becomes inefficient, consistent with reduced Φ_Δ values. The processes described are schematically depicted in Figure 14.

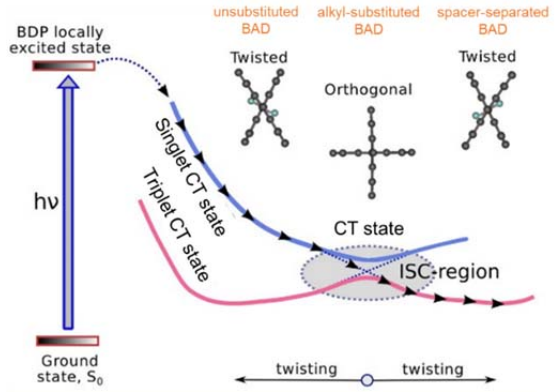

Figure 14. General schematic mechanism of the ISC process in BADs involving S^{BDP}->S^{CT} transition.

Restriction of molecular rotation in a viscous solvent could be expected to decrease ISC in dyads **1**-**3** due to reduced probability of adopting an orthogonal conformation. The effect of viscosity-controlled twisting on the photophysical properties has been studied in details for porphyrin dimers and BODIPY molecular rotors.[50] A large difference in triplet excited state yields between polar (ethanol, DMF) and non-polar (hexane, toluene) solvents, observed for these dyads by transient absorption and $^1O_2$ trapping experiments, could be in part associated with this effect. Under standard conditions, the viscosities of ethanol and hexane are 1.14 and 0.33 mPa, respectively. When measured in more viscous cyclohexane (η = 1.0 at 20°), the Φ_Δ value of dyad **2** dropped to 0.28, compared to hexane (0.38, Table 2) which possesses similar polarity and, consequently, comparable PeT rates. Likewise, in methanol (η = 0.59 at 20°) Φ_Δ increased to 0.15, compared to ethanol (0.05, Table 2).

Conclusions

Overall, in the BAD systems rapid light-induced charge transfer is observed to compete with local fluorescence of the BODIPY's local excited state. Structural factors and media polarity determine the dominant decay pathway. Alkyl substituents effectively attenuate the HOMO energy level of the BODIPY subunit and CT state, making PeT feasible for these dyads in polar solvents. Depending on the energy gap between the S^{BDP} and CT state, the latter species can be formed in high yields. The lifetimes of the CT states are reasonably long, allowing ISC process to take place. This leads to the formation of a local T^{BDP} and T^{Ant} state, as was evidenced by transient absorption studies. The resulting triplets can be used for selective generation of singlet oxygen, depending on the polarity of the medium.

Intersystem crossing in the CT state is promoted by the orthogonal orientation of the subunits in the BADs. Many examples of efficient ISC in orthogonal dyads have been reported, however the nature of this effect had not been clearly identified so far. The present computational study suggests that ISC in such dyads is driven by a reduced S-T energy gap and may take place *via* hyperfine coupling. In order for the $S^{CT} \rightarrow T^{CT}$ transition to be possible, the molecule should stay on the potential energy surface near orthogonal geometry, thereby bringing the S^{CT} and T^{CT} states together. For example, the presence of a separating phenylene unit will lead to free rotation between the BODIPY and anthracene fragments, thus reducing the probability of adopting an orthogonal conformation. As a result, negligible ISC is observed in such dyads.

A particular point of interest in the BADs family discussed here concerns the generation of triplet states and singlet oxygen by dyads **1**-**3**. We suggest that the observed generation of triplet excited states in non-polar solvents is due to lower CT state energies, with respect to BADs with alkyl substituents, which were shown to destabilize CT states. Lower energy gap between S^{BDP} and S^{CT} makes the PeT process feasible, which is consistent with steady-state emission and transient absorption data. In addition, solvent viscosity is likely to affect triplet state formation, as indicated by comparing the Φ_Δ values in solvents of similar polarity but largely different viscosities. This result suggests the possibility of tuning ISC in these dyads by changing solvent viscosity and/or temperature.

Looking forward, we anticipate that the scope of donor-acceptor dyads capable of triplet sensitization mediated by intramolecular charge-transfer is very broad and not limited to systems containing anthracene as an electron donor or BODIPY as an acceptor. Efficient PeT has been reported by Nagano *et al*. in BODIPYs with electron donor phenyl (mono-, di- and trimethoxyphenyl) and naphthalenyl groups.[51] Although ISC in these molecules has not been studied, the observed photophysical properties are consistent with the idea of triplet state formation from CT states. Similar donor-acceptor couplings, resulting in a pronounced solvatochromism were reported by Murgia *et al.* for BODIPY-pyrene dyads.[52] Very recently, Zhang studied photo-induced charge transfer in BODIPY dimers[25] and confirmed that triplet excited state generation takes place through the mechanism presented here, rather than through SO-ISC as previously claimed for such systems.[12] Finally, when this paper was in preparation, Majima *et al.* reported $^1O_2$ sensitization in aggregates formed by electron donor-acceptor fluorescein-anthracene dyads in an aqueous environment,[53] confirming that PeT-mediated triplet state sensitization in not limited to BODIPY derivatives.

Triplet sensitizers based on such dyads possess significant potential for many applications, particularly related to biomedical applications due to the unique polarity-dependent generation of triplet excited states and singlet oxygen. Exploration of these applications requires efficient PeT sensitizers based on synthetically readily accessible dyad molecules and their biocompatible derivatives. Our previously described synthetic approach towards BADs bearing water-solubilizing groups[17] allowed us to elaborate corresponding derivatives of dyads **1**-**16** for *in vitro* and *in vivo* investigation. The results of these studies will be reported elsewhere.

Conflicts of interest

There are no conflicts to declare.

Acknowledgements

This work was supported by grants from the European Commission (CONSORT, Grant No. 655142), Science Foundation Ireland (SFI IvP 13/IA/1894) and the Irish Research Council (GOIPG/2016/1250). The research reported in this publication was supported by funding from King Abdullah University of Science and Technology (KAUST).

Notes and references

1 (a) A. Treibs and F.-H. Kreuzer, *Liebigs Ann. Chem.*, 1968, **718**, 208; (b) A. Loudet and K. Burgess, *Chem. Rev.*, 2007, **107**, 4891.

2 (a) J. Karolin, L. B. A. Johansson, L. Strandberg and T. Ny, *J. Am. Chem. Soc.*, 1994, **116**, 7801; (b) M. S. T. Gonçalves, *Chem. Rev.,* 2009**, 109***,* 190.

3 (a) T. A. Golovkova, D. V. Kozlov and D. C. Neckers, *J. Org. Chem.*, 2005, **70**, 5545; (b) C. Trieflinger, K. Rurack and J. Daub, *Angew. Chem. Int. Ed.*, 2005, **44**, 2288.

4 (a) B. Turfan and E. U. Akkaya, *Org. Lett.,* 2002, **4**, 2857; (b) K. P. Carter, A. M. Young, and A. E. Palmer, *Chem. Rev.*, 2014, **114**, 4564.

5 (a) T. López Arbeloa, F. López Arbeloa, I. López Arbeloa, I. Garcia-Moreno, A. Costela, R. Sastre and F. Amat-Guerri, *Chem. Phys. Lett.*, 1999, **299**, 315; (b) M. J. Ortiz, I. Garcia-Moreno, A. Agarrabeitia, G. Duran-Sampedro, A. Costela, R. Sastre, F. López Arbeloa, J. B. Prieto and I. López Arbeloa, *Phys. Chem. Chem. Phys.*, 2010, **12**, 7804.

6 (a) S. O. McDonnell, M. J. Hall, L. T. Allen, A. Byrne, W. M. Gallagher and D. F. O'Shea, *J. Am. Chem. Soc.,* 2005, **127**, 16360; (b) A. Kamkaew, S. H. Lim, H. B. Lee, L. V. Kiew, L. Y. Chung and K. Burgess, *Chem. Soc. Rev.,*2013, **42**, 77.

7 (a) P. Yang, J. Zhao, W. Wu, X. Yu and Y. Liu, *J. Org. Chem.*, 2012, **77**, 6166; (b) W. Wu, J. Zhao, H. Guo, J. Sun, S. Ji and Z. Wang, *Chem. – Eur. J.*, 2012, **18**, 1961; (c) J. F. Sun, F. F. Zhong and J. Z. Zhao, *Dalton Trans.*, 2013, **42**, 9595; (d) S. Guo, L. H. Ma, J. Z. Zhao, B. Kucukoz, A. Karatay, M. Hayvali, H. G. Yaglioglu and A. Elmali, *Chem. Sci.*, 2014, **5**, 489.

8 (a) T. N. Singh-Rachford, A. Haefele, R. Ziessel and F. N. Castellano, *J. Am. Chem. Soc.*, 2008, **130**, 16164; (b) J. Zhou, Q. Liu, W. Feng, Y. Sun and F. Li, *Chem. Rev.*, 2015, **115**, 395; (c) J. Zhao, W. Wu, J. Sun and S. Guo, *Chem. Soc. Rev.*, 2013, **42**, 5323.

9 J. Zhao, K. Xu, W. Yang, Z. Wang and F. Zhong, *Chem. Soc. Rev.*, 2015, **44**, 8904.

10 J. Zhao, W. Wu, J. Sun and S. Guo, *Chem. Soc. Rev.*, 2013, **42**, 5323.

11 M. Bröring, R. Krüger, S. Link, C. Kleeberg, S. Köhler, X. Xie, B. Ventura and L. Flamigni, *Chem. Eur. J.*, 2008, **14**, 2976.
12 (a) Y. Cakmak, S. Kolemen, S. Duman, Y. Dede, Y. Dolen, B. Kilic, Z. Kostereli, L. T. Yildirim, A. L. Dogan, D. Guc and E. U. Akkaya, *Angew. Chem. Int. Ed.*, 2011, **50**, 11937; (b) S. Duman, Y. Cakmak, S. Kolemen, E. U. Akkaya and Y. Dede, *J. Org. Chem.*, 2012, **77**, 4516.
13 (a) K. Nagarajan, A. R. Mallia, V. S. Reddy and M. Hariharan, *J. Phys. Chem. C*, 2016, **120**, 8443; (b) K. Nagarajan, A.R. Mallia, K. Muraleedharan and M. Hariharan, *Chem Sci.*, 2017, **8**, 1776.
14 S. P. McGlynn, T. Azumi and M. Kinoshita, M. in *Molecular Spectroscopy of the Triplet State*, Prentice Hall, New York, 1969; pp 284-325.
15 (a) P. Spenst, R. M. Young, M. R. Wasielewski and F. Würthner, *Chem. Sci.*, 2016, **7**, 5428; (b) K. M. Lefler, K. E. Brown, W. A. Salamant, S. M. Dyar, K. E. Knowles and M. R. Wasielewski, *J. Phys. Chem. A*, 2013, **117**, 10333; (c) D. Veldman, S. M. A. Chopin, S. C. J. Meskers, M. M. Groeneveld, R. M. Williams and R. A. J. Janssen, *J. Phys. Chem. A*, 2008, **112**, 5846.
16 (a) M. T. Colvin, A. Butler Ricks, A. M. Scott, D. T. Co and M. R. Wasielewski, *J. Phys. Chem. A*, 2012, **116**, 1923; (b) Z. E. X. Dance, S. M. Mickley, T. M. Wilson, A. Butler Ricks, A. M. Scott, M. A. Ratner and M. R. Wasielewski, *J. Phys. Chem. A 2008*, **112**, 4194; (c) Z. E. X. Dance, Q. Mi, D. W. McCamant, M. J. Ahrens, M. A. Ratner and M. R. Wasielewski, *J. Phys. Chem. B*, 2006, **110**, 25163.
17 M. A. Filatov, S. Karuthedath, P. M. Polestshuk, H. Savoie, K. J. Flanagan, C. Sy, E. Sitte, M. Telitchko, F. Laquai, R. W. Boyle and M. O. Senge, *J. Am. Chem. Soc.*, 2017, **139**, 6282.
18 Z. Wang and J. Zhao, *Org. Lett.*, 2017, **19**, 4492.
19 A. P. de Silva, H. Q. N. Gunaratne, T. Gunnlaugsson, A. J. M. Huxley, C. P. McCoy, J. T. Rademacher and T. E. Rice, *Chem. Rev.*, 1997**, 97**, 1515.
20 T. Kowada, H. Maeda and K. Kikuchi, *Chem. Soc. Rev.*, 2015, **44**, 4953.
21 (a) M. Galletta, S. Campagna, M. Quesada, G. Ulrich and R. Ziessel, *Chem. Commun.*, 2005, 4222; (b) M. Galletta, F. Puntoriero, S. Campagna, C. Chiorboli, M. Quesada, S. Goeb and R. Ziessel, *J. Phys. Chem. A*, 2006, **110**, 4348; (c) W. Wu, J. Sun, X. Cui and J. Zhao, *J. Mater. Chem. C*, 2013, **1**, 4577; (d) F. Nastasi, F. Puntoriero, S. Campagna, S. Diring and R. Ziessel, *Phys. Chem. Chem. Phys.*, 2008, **10**, 3982; (e) F. Nastasi, F. Puntoriero, S. Serroni, S. Campagna, J.-H. Olivier and R. Ziessel, *Dalton Trans.*, 2014, **43**, 17647; (f) W. Wu, J. Zhao, H. Guo, J. Sun, S. Ji and Z. Wang, *Chem. Eur. J.*, 2012, **18**, 1961.
22 (a) W. Wu, J. Zhao, J. Sun and S. Guo, *J. Org. Chem.*, 2012, **77**, 5305; (b) R. Ziessel, B. D. Allen, D. B. Rewinska and A. Harriman, *Chem. Eur. J.*, 2009, **15**, 7382; (c) J.-Y. Liu, M. E. El-Khouly, S. Fukuzumi and D. K. Ng, *Chem. Asian J.*, 2011, **6**, 174; (d) A. N. Amin, M. E. El-Khouly, N. K. Subbaiyan, M. E. Zandler, S. Fukuzumi and F. D'Souza, *Chem. Commun.*, 2012, **48**, 206; (e) L. Huang, X. Yu, W. Wu and J. Zhao, *Org. Lett.*, 2012, **14**, 2594.
23 A. C. Benniston, G. Copley, H. Lemmetyinen and N. V. Tkachenko, *ChemPhysChem*, 2010, **11**, 1685.
24 A. Harriman, L. J. Mallon, G. Ulrich and R. Ziessel, *ChemPhysChem*, 2007, **8**, 1207.
25 X.-F. Zhang, X. Yang, B. Xu, *Phys. Chem. Chem. Phys.*, 2017, **19**, 24792.
26 X. He, A. C. Benniston, H. Lemmetyinen and N. V. Tkachenko, *ChemPhotoChem*, 2017, in press.
27 S. Mukherjee and P. Thilagar, *RSC Adv.*, 2015, **5**, 2706.
28 (a) N. Ghoneim and P. Suppan, *Pure Appl. Chem.*, 1993, **65**, 1739; (b) J. Li, Y. Qian, L. Xie, Y. Yi, W. Li and W. Huang, *J. Phys. Chem. C*, 2015, **119**, 2133; (c) Y. Qian, M. Cai, X. Zhou, Z. Gao, X. Wang, Y. Zhao, X. Yan, W. Wei, L. Xie and W. Huang, *J. Phys. Chem. C*, 2012, **116**, 12187.
29 M. Maus and W. Rettig, *J. Phys. Chem. A,* 1999, **103**, 3388.
30 The MO energies for all free molecules were shifted by appropriate constants $\delta_{HOMO/LUMO}$ to match the HOMO/LUMO energies of moieties inside the BAD system. For BODIPY and anthracene fragments $\delta_{HOMO/LUMO}$ = +0.005/+0.004 a.u. and $\delta_{HOMO/LUMO}$ = –0.015/–0.018 a.u. were applied, respectively.
31 J. R. Lakowicz, *Principles of Fluorescence Spectroscopy*, 2nd Ed., Kluwer Academic/Plenum Publishers, New York, London, Moscow, Dordrecht, 1999.
32 G. J. Kavarnos and N. J. Turro, *Chem. Rev.*, 1986, **86**, 401.
33 X.-F. Zhang and X. Li, *J. Lumin.*, 2011, **131**, 2263.
34 E. Gandin, Y. Lion and A. Van de Vorst, *Photochem. Photobiol.*, 1983, **37**, 271.
35 (a) S. Hattori, K. Ohkubo, Y. Urano, H. Sunahara, T. Nagano, Y. Wada, N. V. Tkachenko, H. Lemmetyinen, S. Fukuzumi, *J. Phys. Chem. B*, 2005, **109**, 15368−15375; (b) A. M. Lifschitz, R. M. Young, J. Mendez-Arroyo, V. V. Roznyatovskiy, C. M. McGuirk, M. R. Wasielewski, C. A. Mirkin, *Chem. Commun.*, 2014, **50**, 6850−6852; (c) I. Martini, J. Hodak, and G. V. Hartland, *J. Chem. Phys.*, **1997**, 107, 8064; (d) P. V. Kamat, *J. Phys. Chem.*, 1989, **93**, 859.
36 (a) H. Kotani, K. Ohkubo, S. Fukuzumi, *J. Am. Chem. Soc.*, **2004**, 126, 15999.; (b) T. Miura, Y. Urano, K. Tanaka, T. Nagano, K. Ohkubo, S. Fukuzumi, *J. Am. Chem. Soc.*, **2003**, 125, 8666.
37 K. Kanemoto, A. Fukunaga, M. Yasui, D. Kosumi, H. Hashimoto, H. Tamekuni, Y. Kawahara, Y. Takemoto, J. Takeuchi, Y. Miura and Y. Teki, *RSC Adv.*, **2012**, 2, 5150.
38 (a) R. E. Kellogg, *J. Chem. Phys.*, 1966, **44**, 411; (b) P. Batat, G. Vives, R. Bofinger, R.-W. Chang, B. Kauffmann, R. Oda, G. Jonusauskas and N. D. McClenaghan, *Photochem. Photobiol. Sci.*, **2012**, 11, 1666-1674.
39 In reference 17, please read the sentence, 'fitting of the PB decays at 380 and 400 nm and the rise of BDP−• and Ant+• bands (Figure 1b) yields time constants of 1.15 and 0.54 ps for the EnT and PeT processes, respectively' in page 6283 as 'fitting of the PB decays at 380 and 400 nm and the rise of BDP−• and Ant+• bands (Figure 1b) yields time constants of 0.54 and 1.15 ps for the EnT and PeT processes, respectively'.
40 Z. Wang, J. Zhao, *Org. Lett.*, 2017, **19**, 4492.
41 X.-F. Zhang and N. Feng, *Chem. Asian. J.*, 2017, **12**, 2447.
42 P.V. Kamat, *Langmuir*, 1990, **6**, 512.
43 A. C. Benniston, A. Harriman, V. L. White, M. Zelzer, R. W. Harrington and W. Clegg, *Photochem. Photobiol. Sci.*, **2010**, 9, 1009.
44 N. Gupta, S. I. Reja, V. Bhalla, M. Gupta, G. Kaur and M. Kumar, *J. Mater. Chem. B,* 2016, **4**, 1968.
45 D. M. E. Freeman, A. J. Musser, J. M. Frost, H. L. Stern, A. K. Forster, K. J. Fallon, A. G. Rapidis, F. Cacialli, I. McCulloch, T. M. Clarke, R. H. Friend and H. Bronstein, *J. Am. Chem. Soc.*, 2017, **139**, 11073.
46 F. B. Dias, J. Santos, D. R. Graves, P. Data, R. S. Nobuyasu, M. A. Fox, A. S. Batsanov, T. Palmeira, M. N. Berberan-Santos, M. R. Bryce and A. P. Monkman, *Adv. Sci.*, 2016, 1600080.
47 (a) B. T. Lim, S. Okajima, A. K. Chandra and E. C. Lim, *Chem. Phys. Lett.*, 1981, **79**, 22; b) H. V. Willigen, G. Jones II and M. S. Farabat, *J. Phys. Chem.*, 1996, **100**, 3312.
48 Z. E. X. Dance, S. M. Mickley, T. M. Wilson, A. B. Ricks, A. M. Scott, M. A. Ratner and M. R. Wasielewski, *J. Phys. Chem. A*, 2008, **112**, 4194.
49 T. Ogiwara, Y. Wakukawa and T. Ikoma, *J. Phys. Chem. A*, 2015, **119**, 3415.
50 (a) M. K. Kuimova, M. Balaz, H. L. Anderson and P. R. Ogilby, *J. Am. Chem. Soc.*, 2009, **131**, 7948; (b) A. Vyšniauskas, M. Qurashi, N. Gallop, M. Balaz, H. L. Anderson and M. K. Kuimova, *Chem. Sci.*, 2015, **6**, 5773.
51 H. Sunahara, Y. Urano, H. Kojima and T. Nagano, *J. Am. Chem. Soc.*, 2007, **129**, 5597-5604.

52 C. Caltagirone, M. Arca, A. M. Falchi, V. Lippolis, V. Meli, M. Monduzzi, T. Nylander, A. Rosa, J. Schmidt, Y. Talmon and S. Murgia, *RSC Adv.*, 2015, **5**, 23443.

53 S. Kim, Y. Zhou, N. Tohnai, H. Nakatsuji, M. Matsusaki, M. Fujitsuka, M. Miyata and T. Majima, *Chem. Eur. J.*, 2017, doi: 10.1002/chem.201703686.